Astronomy & Astrophysics

Accretion in the ρ-Ophiuchi pre-main sequence stars[*],[**]

A. Natta, L. Testi, and S. Randich

Osservatorio Astrofisico di Arcetri, INAF, Largo E. Fermi 5, 50125 Firenze, Italy
e-mail: natta@arcetri.astro.it

ABSTRACT

Aims. The aim of this paper is to provide a measurement of the mass accretion rate in a large, complete sample of objects in the core of the star forming region ρ Oph.

Methods. The sample includes most of the objects (104 out of 111) with evidence of a circumstellar disk from mid-infrared photometry; it covers a stellar mass range from about 0.03 to 3 $M_\odot$ and it is complete to a limiting mass of $\sim$0.05 $M_\odot$. We used J and K-band spectra to derive the mass accretion rate of each object from the intensity of the hydrogen recombination lines, Paβ or Brγ. For comparison, we also obtained similar spectra of 35 diskless objects.

Results. The results show that emission in these lines is only seen in stars with disks, and can be used as an indicator of accretion. However, the converse does not hold, as about 50% of our disk objects do not have detectable line emission. The measured accretion rates show a strong correlation with the mass of the central object ($\dot{M}_{\rm acc} \propto M_\star^{1.8\pm0.2}$) and a large spread, of two orders of magnitude at least, for any interval of $M_\star$. A comparison with existing data for Taurus shows that the objects in the two regions have similar behaviour, at least for objects more massive than $\sim$0.1 $M_\odot$. The implications of these results are briefly discussed.

Key words. stars: formation – accretion, accretion disks – stars: activity

1. Introduction

Accretion disks are common around young stars of all mass, from $M_\star \sim 3~M_\odot$ down to very low mass objects and brown dwarfs. They form during the collapse of the molecular core, from which the star is born, and last well beyond this initial phase, when the core has dispersed and the star has acquired most of its final mass. The accretion disks are the birthplace of planets, whose formation and evolution are controlled by the disk physics.

Even if accretion disks have been part of the accepted paradigm of star formation for many years, many of their physical properties are poorly known, and the physical mechanism of angular momentum transfer, which determines the disk evolution, is still unclear. The physical quantity that controls the accretion phase is the mass accretion rate through the disk $\dot{M}_{\rm acc}$. This quantity can be derived only indirectly, by fitting models to observed quantities such as the UV excess emission and/or the profiles and intensity of lines believed to form in the accreting gas. Measurements of $\dot{M}_{\rm acc}$ are now available for a large number of stars in Taurus (e.g., Muzerolle et al. 2005, and references therein). The results have shown that $\dot{M}_{\rm acc}$ is a strong function of the mass of the central object, roughly $\propto M_\star^2$, and that a large dispersion is present (about two orders of magnitude) for objects with the same $M_\star$. Both results are a challenge for accretion disk models, as discussed, e.g., by Muzerolle et al. (2003) and Natta et al. (2004).

Measurements of accretion rates in other star forming regions are scarce in comparison, mostly limited to very low mass

objects (Muzerolle et al. 2003, 2005). In a study of very low mass objects and brown dwarfs in Ophiuchus, Natta et al. (2004) found that they are actively accreting with $\dot{M}_{\rm acc}$ higher by at least one order of magnitude than objects of similar mass in Taurus. This could be due to a difference in age, since the Ophiuchus BDs are very young objects, younger than their Taurus counterparts, but could also be due to different environmental conditions.

While it is clearly necessary to improve the physical models of accretion disks, at the same time it is important to study large and if possible complete samples of stars in a variety of star forming regions, differing in age and global properties.

We report in this paper the results of a project aimed at measuring the mass accretion rate of a large sample of pre-main sequence objects, ranging from a few solar masses to few tens of Jupiter masses, in the star forming region ρ Oph. The core of ρ Oph is perfectly suited for such a study, as it is rich in pre-main sequence stars, which include intermediate mass objects, T Tauri stars (TTS) and brown dwarfs (BDs). Its stellar content has been studied, e.g., by Luhman & Rieke (1999, LR99 in the following, and references therein to previous work), Natta et al. (2002) and, more recently, by Wilking et al. (2005). Moreover, ρ Oph is very different from Taurus, younger and more compact, and it will allow us to explore the accretion properties of pre-main sequence stars under different conditions, following the results of Natta et al. (2004).

Ophiuchus has been observed in two mid-IR bands with ISO by Bontemps et al. (2001, BKA01 in the following), who detected 199 sources in the ρ Oph core. Of these, 111 were classified, on the basis of their IR colors, as Class II objects, i.e., visible young stellar objects with evidence of disks. They provide a sample of systems with disks *complete* to a limiting mass of about 0.05 $M_\odot$. In a spectroscopic study of the very low

---

luminosity objects of the BKA01 sample, Natta et al. (2002) confirmed that they were BDs with mid-IR excess, very likely from a circumstellar disk; as mentioned, these BDs show significant differences in accretion properties from their analogs in Taurus.

The disadvantage of observing ρ Oph is its high extinction, which makes veiling measurements in the UV and visual impossible except for a few objects. The most effective way to determine $\dot{M}_{acc}$ for the Ophiuchus sample is therefore to use the luminosity of hydrogen recombination lines, such as Paβ and/or Brγ. The relation between IR line luminosity and accretion luminosity, independently measured from the UV excess, was established by Muzerolle et al. (1998b) for TTS, and by Calvet et al. (2004) for intermediate mass objects. Natta et al. (2004) extended it to very low mass objects, where $\dot{M}_{acc}$ was determined by fitting the observed Hα profiles with the predictions of magnetospheric accretion models.

In this paper, we present the results of a spectroscopic IR survey of Ophiuchus objects. In Sect. 2, we describe the properties of the observed sample, which includes almost all (104 out of 111) the Class II objects and a subset (35 objects out of 77) of the diskless systems (Class III), also from the BKA01 survey, that we will use for comparison. The observations, data reduction and method of analysis are discussed in Sect. 3. The results are presented in Sect. 4 and discussed in Sect. 5. Section 6 summarizes our conclusions.

2. Characteristics of the observed sample

2.1. The sample

The most complete survey of young stellar objects in the ρ Oph Main Cloud (L 1688) is that obtained in two mid-IR bands (6.7 and 15.3 μm) with ISOCAM (BAK01). Based on the near and mid-IR colors, the objects were divided in Class I (accreting protostars), Class II and tentative Class II (pre-main sequence stars with IR excess typical of disks, like classical T Tauri stars or CTTS), and Class III/tentative Class III (objects with colors typical of stellar photospheres, like weak-line T Tauri stars or WTTS). BAK01 estimate that their Class II sample of 111 objects is complete to a limiting luminosity $L_\star \sim 0.03\ L_\odot$, corresponding approximately to 0.05 $M_\odot$. The Class III sample is only complete to $\sim$0.2 $L_\odot$ (about 0.15 $M_\odot$). Note that not all the Class III objects have been confirmed as ρ Oph members. Barsony et al. (2005) have recently confirmed the accuracy of the ISOCAM results with ground-based 10 μm observations of a large subset of the BKA01 sources.

Our sample includes 104 of the 111 Class II/tentative Class II objects (Class II for simplicity in the following) listed by BAK01 in the ρ Oph core. Most of the spectra (96) were obtained in the J band; the remaining 8, of objects too weak in J, in the K band; one object has been observed at both wavelengths. As a comparison sample, we observed 35 of the 77 Class III and tentative Class III (in the following, Class III) objects, 31 in the J band and 4 in K. The objects and their properties are listed in Tables C.1 and C.2.

2.2. Stellar parameters

The stellar properties (i.e., spectral type, luminosity, mass and radius) of the BAK01 sample are well known only for a handful of objects. The main difficulty comes from the large uncertainties that affect spectral types, due to the combination of high extinction and large veiling, even at near-IR wavelengths

(e.g., LR99 and references therein; Doppman et al. 2003; Wilking et al. 2005). LR99, using K-band low resolution spectra, provide spectral types for 37 of our Class II objects. However, 23 of them have uncertainties of almost one spectral class.

Given the uncertainties, and considering that most of our objects do not have any spectral classification, we have decided to adopt a statistical approach, following BAK01.

First, we compute the extinction toward each object from the observed $(J - H) - (H - K)$ colors, as given by 2MASS[1], corrected to CIT system, adopting the Ophiuchus extinction law of Kenyon et al. (1998) and the locus of CTTS defined by Meyer et al. (1997). The result can be expressed as:

$$A_J = 2.31\left(1.72\,(J-H)_{CIT} - (H-K)_{CIT} - 0.896\right). \qquad (1)$$

This relation gives the correct reddening also for objects with no excess in the near infared, as long as they have $T_{eff} \lesssim 5000$ K (spectral type later than K2), which applies to the majority of our sample. However, for diskless objects of earlier spectral type it will underestimate A_J and thus the inferred $L_\star$ significantly. We will come back to this point in Sect. 4.1.

The stellar luminosity is computed from the J magnitude and A_J, using a bolometric correction similar to that adopted by BAK01:

$$\log L_\star = 1.24 + 1.1 \log L_J \qquad (2)$$

where $L_\star$, L_J are in units if $L_\odot$ and $L_J = 301 \times 10^{-(J-A_J)/2.5}$. Equation (2) assumes that the J-band disk emission is negligible in comparison to the photospheric one. If this is not the case, the equation overestimates $L_\star$. A recent work by Cieza et al. (2005) suggests that classical TTS have a J-band excess of $\sim$0.3 mag on average, so that $L_\star$ derived from the J magnitude is higher than the true one by about 30%. We have checked that, if such a correction applies to objects of all masses, none of our conclusions will change. Our values of $L_\star$ are in agreement with LR99 estimates always within a factor of 2, and generally much better. We have also compared the luminosities derived in this way with the results obtained by Natta et al. (2002) from near-infrared J, H, K low resolution spectroscopy for a group of 10 BDs; also in this case, the results are within a factor of 2, with the exception of one object (ρOph-ISO 033), for which we underestimate the luminosity by almost one order of magnitude. This discrepancy has no impact on the results of this paper.

When only H and K magnitudes were available (17 Class II and 1 Class III objects), we estimated the stellar luminosity using Eqs. (2) and (4) of BKA01.

There are 5 objects (4 Class II and 1 Class III) that have companions clearly seen in our spectra, but which are not resolved in the 2MASS photometry. All the companions have a good detection of the continuum; the flux ratio between the primary and the secondary is always larger than a factor of 3. Two of the companions (ρOph-ISO 068b and ρOph-ISO 072b) have been detected in the K-band ρ Oph multiplicity survey of Ratzka et al. (2005), with flux ratios to the primary of 0.19 and 0.16, respectively. We have accordingly not corrected the 2MASS magnitudes of the primaries for the contribution of the companions, because the corrections to the derived parameters would have been within the uncertainties. The secondary components have no detectable

---

[1] This publication makes use of data products from the Two Micron All Sky Survey, which is a joint project of the University of Massachusetts and the Infrared Processing and Analysis Center/California Institute of Technology, funded by the National Aeronautics and Space Administration and the National Science Foundation.

Paβ emission, and we will omit them from our analysis in the following; their properties are summarized in Table C.3.

To determine stellar radii and masses, we make the assumption that the star formation in Ophiuchus is coeval, and that all the objects lie on a single isochrone in the HR diagram. With this assumption, we can derive stellar mass, temperature and radius from the measured $L_\star$. This procedure is reasonable for the Ophiuchus core, whose age estimates range between 0.5 and 1 Myr, with very few stars older than that (BAK01; LR99). In the following, we adopt the D'Antona & Mazzitelli (1997 and 1998 web updates; DM98 in the following) evolutionary tracks for an age of 0.5 My. The uncertainties introduced by the assumption of coeval star formation and the differences expected if other evolutionary tracks were used are discussed in Appendix A.

The values of the stellar parameters are given in Tables C.1 and C.2.

3. Observations and data analysis

3.1. Observations and data reduction

Near infrared moderate resolution J and K band spectroscopic observations of all targets in our sample were obtained at the ESO Observatories in Chile. The objects were either observed using the SofI instrument at the NTT 2.2 m telescope (June 2004, Visitor Mode) or the ISAAC instrument at the Antu 8.2 m VLT unit telescope (Spring 2004, Service Mode), as specified in Tables C.1 and C.2. Detailed descriptions of both these instruments are available on the ESO web pages[2]. For all the objects that were observable at J-band, with SofI we used the 0.6 arcsec slit and the Blue low resolution grims, resulting in a spectral resolution of approximately $\lambda/\Delta\lambda \sim 1000$ and a spectral coverage from ~0.95 to ~1.64 μm; with ISAAC we employed the short-wavelength low resolution spectral mode with central wavelength 1.25 μm and 0.6'' slit width, giving a spectral resolution of $\lambda/\Delta\lambda \sim 900$ and a spectral coverage limited to the J-band. A number of objects were only observable at K-band, for these we either used the SofI Red low resolution grism with similar spectral resolution as for the Blue grism observations and spectral coverage from ~1.6 to 2.5 μm, or the ISAAC short wavelength low resolution mode with central wavelength 2.2 μm, which offers a similar spectral resolution as the J-band observations and a spectral coverage limited to the K-band. Integration times varied from about 0.5 to 2 h on source, depending on the expected brightness of the objects and observing conditions (in Visitor Mode).

During the Visitor Mode observations at the NTT telescope, we acquired several telluric standard stars per night at varying airmasses; each Observing Block from our programme executed in Service Mode at the VLT was preceded or followed by a telluric standard observed with the same instrument mode and at a similar airmass as our target stars. Spectroscopic flat fields and arcs were obtained during daytime either before or after our observations. Standard methods were employed to calibrate our data. We did not attempt to obtain flux calibrated spectra; all our spectra are wavelength calibrated using OH airglow lines and corrected on an arbitrary intensity scale for telluric absorption and instrument response using the telluric standard star observations.

Correction for telluric absorption and instrumental response was obtained observing at similar airmasses early type stars

(early B or O) of known spectral type from the telluric standards lists of ISAAC[3]. These stars all have Paβ or Brγ absorption which were manually removed from the spectra before applying the correction.

Most of the spectra are of excellent quality; the detection limits of the Paβ or Brγ equivalent width are in general of the order of 0.5−1 Å. Variations around this limit are mainly related to the signal to noise ratio achieved on the photospheric continuum of the individual objects. The signal to noise ratio depends on the telescope/instrument used, the observing conditions, the integration time and the apparent magnitude of the object. It is not necessarily a function of the object intrinsic luminosity because the extinction can be very different and because we tried as much as possible to observe two objects at the same time by properly aligning the slit, so that some relatively bright source near a faint one may have been observed with ISAAC and a long integration time. However, most of the lower luminosity objects have been observed with ISAAC and, expecting lower line intensities, with a higher signal to noise ratio; thus, the line detection limits for low luminosity objects are generally lower than for intermediate luminosity ones.

The sample studied in this paper includes also the 9 BKA01 sources for which Natta et al. (2004) obtained J and K band spectra with ISAAC. We have taken the Natta et al. (2004) J band spectra and reanalyzed them in the same manner used for the others.

3.2. Method

The luminosity of Paβ and Brγ are computed from the measured equivalent widths of the emission lines and the broad-band J and K fluxes, corrected for extinction, determined as described in Sect. 2.2. No correction for underlying photospheric absorption was applied, since the expected equivalent width is small ($\lesssim 0.5$ Å; Wallace et al. 2000) for objects with $T_{\rm eff} \lesssim 5000$ K, which represent the quasi-totality of our sample (see Table C.1) and would not change the results.

There are 12 Class II (11 of them have no Paβ detection) for which it was not possible to determine line fluxes, due to lack of J magnitudes; they will not be included in the following discussion. Similarly, we will not consider further the one Class II (ρOph-ISO 035) with weak Paβ in absorption.

The accretion luminosity of each Class II object is derived from the empirical correlation between $L_{\rm acc}$ and the luminosity of Paβ or Brγ, derived by Natta et al. (2004) and Calvet et al. (2004), respectively (see also Muzerolle et al. 1998b):

$$\log L_{\rm acc}/L_\odot = 1.36 \log L({\rm P}_\beta)/L_\odot + 4 \tag{3}$$
$$\log L_{\rm acc}/L_\odot = 0.9\,(\log L({\rm Br}_\gamma)/L_\odot + 4) - 0.7. \tag{4}$$

These relations have been calibrated using accretion luminosities derived by fitting the measured veiling (for T Tauri stars) and/or H$_\alpha$ profiles with the predictions of magnetospheric accretion models; the objects used for the calibration cover the mass range from ~3 $M_\odot$ to brown dwarfs. The mass accretion rate is then computed from $L_{\rm acc}$ ($\dot{M}_{\rm acc} = L_{\rm acc}\,R_\star/(GM_\star)$). The results are given in Table C.1.

The reliabilty of our procedure was verified by applying it to a sample of well studied pre-main sequence stars, covering roughly the same range of masses, for which reliable values of the stellar parameters (i.e., mass and radius) and of the accretion
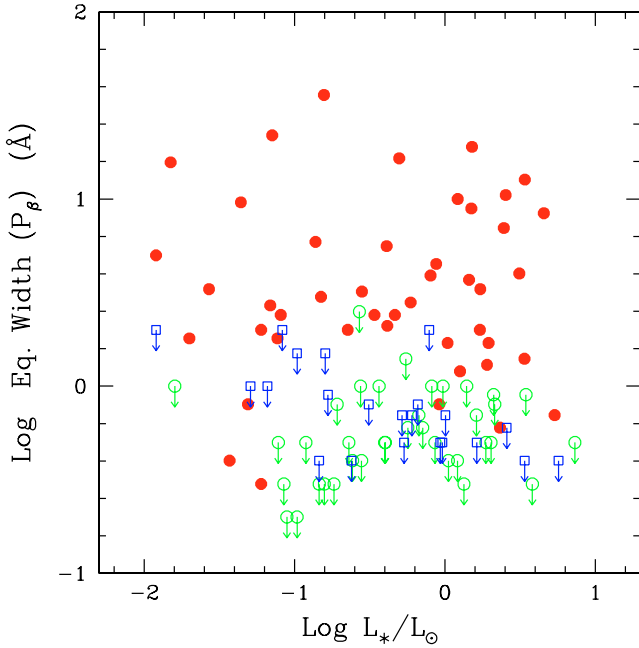
Fig. 1. Equivalent width of the Paβ emission line for all objects with known $L_\star$. Circles are Class II sources, filled circles are detections, empty circles with arrows upper limits. Squares are Class III sources. Two objects with $L_\star < 0.01\ L_\odot$ and Paβ undetected are not plotted.

Fig. 2. Accretion luminosity from the IR lines as function of $L_\star$ for Class II objects. Dots show L_{acc} measurements from Paβ (filled: detections, empty: upper limits); diamonds measurements from Brγ (filled: detections, empty: upper limits); The dotted lines show the locus of $L_{acc}/L_\star = 0.01$, 0.1 and 1, as labelled. Crosses are objects in Taurus (see text for references).

rate could be found in the literature. Using literature measurements of the Paβ intensity and of $L_\star$, we derived for each object mass and accretion rate as done for the Ophiuchus objects, and compared them to the "real" values. Details can be found in the Appendix B.

We have applied a similar procedure to the Class III objects; the results are shown in Table C.2.

4. Results

4.1. Equivalent widths

Emission in the near-IR hydrogen recombination lines has been detected in 45% of Class II sources, 46 of the 96 observed in Paβ and 1 out of 9 observed in Brγ. In contrast, no Class III source shows emission in these hydrogen lines; 8 Class III objects have Paβ or Brγ in absorption and for the others we do not see the lines. The measured equivalent widths are given in Tables C.1 and C.2. Figure 1 shows the Paβ equivalent width as function of $L_\star$.

Six Class III objects have Paβ in absorption with equivalent widths $\gtrsim 1$ Å, i.e., larger than one can expect in late-type stars (Wallace et al. 2000). They are likely earlier type stars, and this is certainly the case of ρ Oph-ISO 180, which is classified A7 by Wilking et al. (2005) and of ρ Oph-ISO 113, earlier than F8 according to LR99. For these six stars, as already mentioned, the method used to estimate A_J and all the derived stellar parameters is not correct; therefore, we omit their stellar parameters from Table C.2.

The comparison between the Class II and Class III samples clearly shows that emission in the near-IR hydrogen lines, in contrast to that in optical lines such as Hα is restricted to objects with circumstellar disks, and can therefore be used as a reliable accretion indicator. However, one should keep in mind that the opposite is not necessarily true, as about 50% objects with disks have no detected emission.
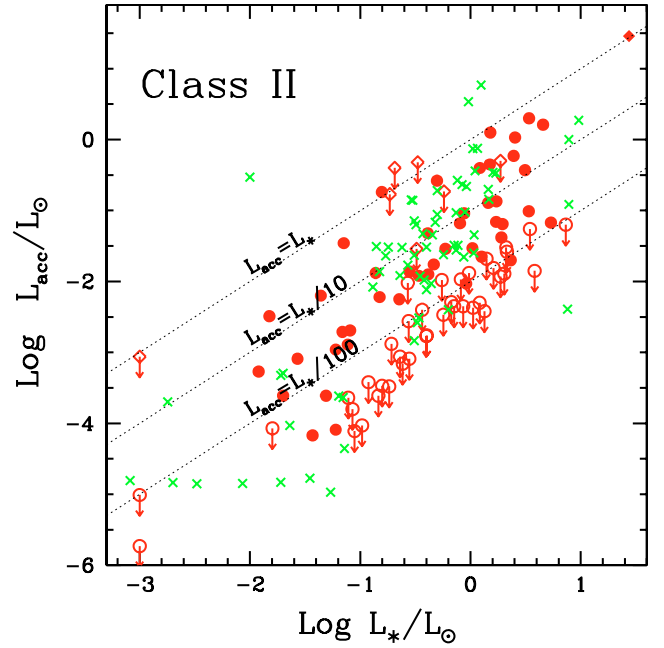
The fraction of Class II objects with detected Paβ emission varies from 56% for $L_\star \gtrsim 1\ L_\odot$ to 42% for $0.03 \lesssim L_\star \lesssim 1\ L_\odot$. Very low luminosity objects (7 objects with $L_\star \lesssim 0.03\ L_\odot$) have a marginally higher detection rate ($\sim$57%), due in part to the sensitivity limit of our measurements, which is higher for lower luminosity objects (see Sect. 3.1), but also due to the incompleteness of the BKA01 survey for very low luminosity sources, which are detected only when they have a large mid-IR excess, very likely indicative of higher accretion rates.

4.2. Accretion luminosity

Figure 2 shows the accretion luminosity of Class II objects computed from the IR line luminosity as a function of $L_\star$.

For any given $L_\star$, there is a large range of measured L_{acc} (about 50), which does not seem to vary significantly with $L_\star$; because of our sensitivity limit, this is probably just a lower limit to the actual range of L_{acc}. One can also see that for the majority of objects $L_{acc}/L_\star < 0.1$, but there is a significant fraction of cases with $L_{acc} \sim L_\star$.

4.3. Mass accretion rate

Figure 3 shows the mass accretion rate $\dot{M}_{acc}$ of Class II sources as function of $M_\star$. There is a clear trend of increasing $\dot{M}_{acc}$ with increasing $M_\star$. Not including upper limits, we find using ASURV (Feigelson and Nelson 1985) $\dot{M}_{acc} \propto M_\star^{1.8\pm0.2}$; the slope does not change if we include the upper limits in the analysis.

Superimposed on this trend, there is a large spread of $\dot{M}_{acc}$ for any value of $M_\star$, of two orders of magnitude at least. Within statistical fluctuations, the objects are distributed quite uniformly in this range.
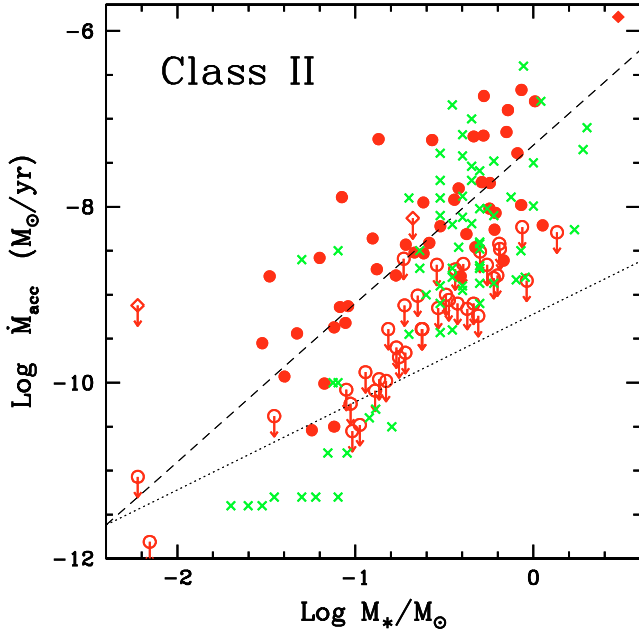
Fig. 3. Mass accretion rate derived from the IR lines as function of $M_\star$. Symbols as in Fig. 2. The dashed line shows the relation $\dot{M}_{\rm acc} \propto M_\star^{1.8}$, derived from a statistical analysis using ASURV; the dotted line plots, for comparison, the relation $\dot{M}_{\rm acc} \propto M_\star$.

5. Discussion

The results summarized in Fig. 3 describe the accretion properties of the largest sample of Class II stars in any single star-forming region studied so far. The sample contains more than hundred objects with evidence of disks, and is complete in the mass interval from $\sim$0.03 to about 3 $M_\odot$. The corresponding accretion rates vary from $\sim 10^{-11}$ to $\sim 10^{-6}$ $M_\odot$/yr, with a strong dependence of $\dot{M}_{\rm acc}$ on $M_\star$ ($\dot{M}_{\rm acc} \propto M_\star^{1.8\pm0.2}$). For any $M_\star$, there is a large dispersion of values of $\dot{M}_{\rm acc}$, of two orders of magnitude at least, which does not seem to change with $M_\star$. Note that the real spread is likely bigger, because of the many upper limits in our survey.

5.1. Ophiuchus and Taurus

One of the aims of our study was to compare the accretion properties in Ophiuchus with those of objects in Taurus. The Taurus results are shown by crosses in Figs. 2 and 3. The accretion luminosity and mass accretion rate have been derived from the UV and optical veiling and/or by fitting with magnetospheric accretion models the Hα profile. This second method is the only possible one for very low mass objects and BDs, since veiling cannot be detected below a limiting value $\dot{M}_{\rm acc} \lesssim 10^{-10}$ $M_\odot$/yr. The results are from Gullbring et al. (1998), Muzerolle et al. (1998b, 2003, 2005), White & Ghez (2001), White & Basri (2003), and Calvet et al. (2004); note that, for homogeneity, we have re-determined $M_\star$ using DM98 tracks for all objects.

The methods used to derive $L_{\rm acc}$ and $\dot{M}_{\rm acc}$ in the two regions are therefore different, since in Ophiuchus $\dot{M}_{\rm acc}$ is derived from the luminosity of the hydrogen recombination lines. However, the relations (Eqs. (3) and (4)) we used have been "calibrated" mostly using Taurus objects (see, e.g., Muzerolle et al. 1998b; Calvet et al. 2004; Natta et al. 2004), so that we do not expect any systematic difference in the Ophiuchus-Taurus comparison due to the different methods.

The two figures show that the accretion properties of the two star forming regions are very similar. Muzerolle et al. (2005) derive $\dot{M}_{\rm acc} \propto M_\star^{2.1}$ for their sample (mostly in Taurus, with additional brown dwarfs from other star-forming regions), neglecting upper limits. Within the errors, this relation is identical to what we obtain in Ophiuchus. If we concentrate in Fig. 3, we can see that not only the slope of the relation of $\dot{M}_{\rm acc}$ with $M_\star$, but also the range of values is very similar. In particular, the two samples have similar values of the maximum $\dot{M}_{\rm acc}$ for any given $M_\star$, and similar spread of $\dot{M}_{\rm acc}$ values, at least for $M_\star \gtrsim 0.06-0.08$ $M_\odot$.

For lower $M_\star$, most Taurus BDs have very low accretion rates, $1-2$ orders of magnitude lower than similar objects in Ophiuchus. As already discussed, the fact that we do not find these very low accretors in Ophiuchus most likely reflects the incompleteness of the BAK01 sample at very low masses, and selects objects with comparatively strong mid-IR fluxes. Natta et al. (2002) showed that the BAK01 sample of brown dwarfs has relatively large luminosity, and is probably very young. As discussed in Sect. 4.1, a fraction larger than for more luminous objects has detected Paβ. All this indicates that there may be low $\dot{M}_{\rm acc}$ BDs which are missing from the Ophiuchus sample. It is, in a way, more surprising that very few, if any, of the brown dwarfs in Taurus have high $\dot{M}_{\rm acc}$, while higher mass objects in the two regions have very similar accretion properties. It is possible that this difference between the two regions at the very low end of the $M_\star$ distribution contains important information, that needs further investigation. This is, however, beyond the scope of this paper.

5.2. Variability

All pre-main sequence stars are variable objects, and, in particular, all the accretion indicators in TTS and BDs show large variability.

Variability does not affect the correlation of $\dot{M}_{\rm acc}$ with $M_\star$, as the ρ Oph sample is sufficiently large that individual fluctuations cannot change it. It may be more important when we consider the spread of $\dot{M}_{\rm acc}$ values for any given $M_\star$. Recently, Scholz & Jayawardhana (2005) have studied the variability of accretion indicators (mostly Hα) for six young brown dwarfs; they claim that the accretion rate in some of their objects varies by at least one order of magnitude, and that this variability may account for the large spread in the $\dot{M}_{\rm acc}-M_\star$ correlation.

We have estimated the magnitude of the spread in $\dot{M}_{\rm acc}$ for individual objects by looking at the results of Gatti et al. (2006), who have recently obtained J-band spectra of a small (14 objects) subset of our Ophiuchus sample. The Gatti et al. sample includes both TTS and BDs, observed one to two years later than the spectra discussed in this paper. The two data sets show variations in the Paβ equivalent width of a factor of two at most (in both directions), with only one exception, where the Paβ equivalent width has increased by a factor of three over the time interval between the two sets of observations. For the same objects, we have also looked in the literature for variations of the broad-band J magnitude, used to compute the line flux (Sect. 3.2). The variation of $\dot{M}_{\rm acc}$, computed taking the maximum variations in the J magnitude and in the Paβ equivalent width, is of a factor $\sim$4. This is much smaller than the dispersion of points in Fig. 3 and would not change significantly any of our conclusions.

A detailed analysis of the variability of the IR emission lines and continuum, in analogy to what has been done for Hα (e.g., Johns-Krull & Basri 1997), is certainly needed. However, from the results obtained so far, it seems unlikely that the dispersion of $\dot{M}_{\rm acc}$ values can be accounted for by variability alone, and that,

if averaged over a sufficiently long period of time, one would find that all the ρ Oph stars of a given mass accrete at the same rate.

5.3. Viscous disks

The $\dot{M}_{acc}$ dependence on $M_\star$ is difficult to understand in terms of disk physics, as discussed, e.g., by Muzerolle et al. (2003), Natta et al. (2004), Calvet et al. (2004). In a standard steady accretion disk model, $\dot{M}_{acc}$ is proportional to the disk mass divided by the time scale for viscous evolution. In an α-disk (Shakura & Sunyaev 1973), the viscosity depends on the ratio Ω/c_s^2, where Ω is the keplerian angular velocity and c_s the sound speed; then, $\dot{M}_{acc} \propto M_d \times M_\star^{-1/2} \times T_d$, where M_d and T_d are disk mass and temperature, respectively. With the further assumptions that $M_d \propto M_\star$ (e.g., Natta et al. 2000), and that the disk heating is dominated by the stellar irradiation, this gives, to zero order, $\dot{M}_{acc} \propto M_\star^{1/2} \times T_\star$. For PMS stars, the relation between $T_\star$ and $M_\star$ is rather shallow (approximately $T_\star \propto M_\star^{0.4}$ for $M_\star \gtrsim 0.1\ M_\odot$, and much flatter for lower masses; see, e.g., DM98) and we expect $\dot{M}_{acc}$ to increase roughly as $M_\star^\gamma$, with $\gamma \lesssim 1$. The relation will be even flatter if the contribution of the stellar radiation to the disk heating is negligible.

It is possible that α (or, more generally, the efficiency of momentum transfer) depends, in turn, on $M_\star$. If viscosity is the result of magneto-rotational instabilities (MRI) (see, e.g., Balbus & Hawley 1991), the disk gas should be sufficiently ionized. Muzerolle et al. (2003) suggest that the steep correlation of $\dot{M}_{acc}$ with $M_\star$ can be explained if the disk ionization is controlled by the X-ray radiation from the star, since the X-ray luminosity is not constant over the mass spectrum, but is observed to increase with $M_\star$.

X-ray observations of Ophiuchus have been recently carried out with Chandra and XMM satellites by Imanishi et al. (2001) and Ozawa et al. (2005). Both studies detected a significant fraction of Class II sources (70 and 48 % respectively); they found that the X-ray spectral properties, as well as the relationship between L_X and L_{bol} of class II sources are similar to those of class III sources, but did not investigate the behaviour of X-ray luminosity with stellar mass. To our knowledge, the only study addressing the relation between mass and X-ray luminosity for young stars over a large range of luminosities and masses is in Orion. The COUP Chandra observations of Orion show that L_X scales approximately as $M_\star^{1.1-1.4}$ in the interval $0.1-2\ M_\odot$ (Preibisch et al. 2005). However, it is not clear that this variation of L_X is sufficient to produce the observed $\dot{M}_{acc}-M_\star$ correlation, and more detailed MRI models, which include X-ray ionization, are required. If the X-ray emission of the central star is controlling accretion, the large spread of L_X observed in the COUP data could also explain the large spread of $\dot{M}_{acc}$ for any given $M_\star$.

Viscous disk models predict that $\dot{M}_{acc}$ decreases with time (e.g., Hartmann et al. 1998). Calvet et al. (2000) estimate $\dot{M}_{acc} \propto t^{-1.5}$, with a large uncertainty, from a sample of TTS in Taurus, Chamaeleon and Ophiuchus. Neither the similarity of accretion rates between Ophiuchus and Taurus nor the very large spread observed in both regions support age as a main factor in the determination of $\dot{M}_{acc}$. If the Calvet et al. (2000) rate is correct, the difference in age between Taurus and Ophiucus should give on average a difference in $\dot{M}_{acc}$ of a factor $\gtrsim 3$, of which we have no evidence. In addition, the Ophiuchus $\dot{M}_{acc}$ range of more than two orders of magnitude corresponds to an age range of at least a factor 20, much too large when compared to the HR location of the objects (see, e.g., LR99).

The time evolution of viscous disks is influenced by the presence of close companions (see Calvet et al. 2000). Companions truncate the circumstellar disk at a radius which depends on the binary separation. As the disk evolves, more and more matter expands outside the truncation radius, with the effect of decreasing the disk mass and $\dot{M}_{acc}$. A sample of objects with the same initial value of $\dot{M}_{acc}$ but companions at different distances will show with time an increasing spread of $\dot{M}_{acc}$ values.

This effect, however, is not seen in the Taurus TTS (White & Ghez 2001), where the accretion rate is similar for single and primary stars with companions as close as 10 AU. At the age of Ophiuchus, only very close companions have had time to reduce $\dot{M}_{acc}$ by a significant factor (separation $\lesssim 30$ AU or $\lesssim 0.2$ arcsec for an age of 10^6 years according to Calvet et al. 2000). There have been a number of multiplicity surveys of Ophiuchus, some capable of detecting very close binaries. Three Class II objects (i.e., objects with a mid-IR detected circumstellar disk) have companions closer than $\lesssim 0.25$ arcsec (Barsony et al. 2005; Ratzka et al. 2005); one has detected Paβ, while in the other two cases the line has not been detected. The observational evidence of a correlation between the accretion rate and the presence of very close companions is clearly inconclusive. At this stage, it cannot be quantitatively confirmed nor dismissed, and should be investigated further.

5.4. Initial conditions

Although all the effects discussed so far can play a role and need further investigation, it is possible that differences in the initial conditions, i.e., in the physical properties of the molecular cores from which the star+disk system forms, determine the TTS disk properties, and in particular the behaviour of $\dot{M}_{acc}$ disussed in this paper.

The self-similar viscous disk models of Hartmann et al. (1998) show that the accretion rate is proportional to the disk mass at $t = 0$, i.e., when accretion onto the disk stops, and, in the early phases ot the evolution, to its $t = 0$ outer radius, which in turns depend on the core properties. Alexander & Armitage (2006) have started exploring how this can introduce a $\dot{M}_{acc} \propto M_\star^2$ correlation at a later time.

More realistic models that follow the formation and evolution of circumstellar disks (Hueso & Guillot 2005) illustrate clearly how different core properties (in particular, different rotation velocities) can create a large spread of $\dot{M}_{acc}$ for objects with the same $M_\star$ and age.

Models that compute the evolution of disks starting from the core infall phase over a large range of parameters are required, if we want to estimate the effect of the initial conditions on the relation of $\dot{M}_{acc}$ with $M_\star$ and on its scatter. The observations presented in this paper, and the similar results for Taurus, provide an excellent test of such models. Note that the the fact that disk accretion properties in Taurus and Ophiuchus are very similar, while the two regions have large differences in their environment, should put strong constraints on these models, which will be interesting to explore fully.

6. Summary and conclusions

In this paper, we report the results of a near-IR spectroscopic survey of a large sample of very young objects in the ρ Oph core. The sample includes all Class II objects, i.e., objects with evidence of circumstellar disks from mid-IR photometry (BKA01). This sample covers the mass range between about 0.03 to 3 $M_\odot$;

according to BKA01, it is *complete* to a limiting magnitude of about 0.03 $L_\odot$, or 0.05 $M_\odot$. We have also observed a significant fraction of Class III objects, i.e., with no mid-IR excess emission, covering a similar range of luminosities.

In contrast to the Balmer lines, the near-IR hydrogen recombination lines are seen in emission only in Class II objects. Of all our Class III sample, none has detected Paβ emission. This confirms our assumption (Natta et al. 2004) that the near-IR lines can provide an immediate indication of the accreting properties of young stars, even when only relatively low resolution spectra are available.

We have derived the mass accretion rate $\dot{M}_{\rm acc}$ from the luminosity of the hydrogen recombination lines, mostly from Paβ but in few cases from Brγ. In total, we obtain measurements of $\dot{M}_{\rm acc}$ for 45 Class II objects, and upper limits for 39.

Our results show that $\dot{M}_{\rm acc}$ increases sharply with $M_\star$ ($\propto M_\star^{1.8\pm0.2}$). We also find a large range of values of $\dot{M}_{\rm acc}$ for any given value of $M_\star$ (a spread of roughly two order of magnitudes, independent of $M_\star$). As discussed in the text, this is likely a lower limit to the true dispersion.

When compared to accretion measurements in Taurus (see Muzerolle et al. 2005, and references therein), we find that the two regions look very similar, at least for objects with $M_\star \gtrsim$ 0.1 $M_\odot$. For both Taurus and Ophiuchus, the dependence of $\dot{M}_{\rm acc}$ on $M_\star$, the upper envelope of the $\dot{M}_{\rm acc}$ distribution (i.e., the largest values of $\dot{M}_{\rm acc}$ that any object of a given mass seems able to sustain), and the range of $\dot{M}_{\rm acc}$ values for any given $M_\star$, are very similar. At lower mass, the accretion rates of the Ophiuchus objects are much larger than their Taurus analogs.

The observed behaviour of $\dot{M}_{\rm acc}$ does not have an obvious explanation. The correlation of $\dot{M}_{\rm acc}$ with $M_\star$ may be due to a dependence of the disk physics on the properties of the central star. Muzerolle et al. (2003) suggest as a cause the effect of the X-ray emission from the central star on the disk ionization and angular momentum transfer. It is also possible that the correlation reflects the properties of the pre-stellar cores, from which the star and disk form. Both possibilities need to be explored further.

The large spread of values of $\dot{M}_{\rm acc}$ for any $M_\star$ may be a side-product of the same mechanisms that produce the correlation between these two quantities, as discussed in Sect. 5. In addition, other effects may play an important role, for example the dynamical action of close companions, or the intrinsic variability of the accretion process.

Appendix A: Testing the assumption of coeval star formation

The assumption of coeval star formation, albeit quite reasonable for a region like ρ Oph, introduces errors in our results. The same is true of the choice of any specific set of evolutionary tracks. However, it turns out that both kinds of errors are unimportant, when dealing with a large sample of objects as in our case.

Figure A.1 shows the analog of Fig. 3, reproduced on the top-left panel, computed using the DM98 isochrone for 1 My and the evolutionary tracks of Siess (2000) for 0.5 My and 1 My, respectively. Older tracks give slightly lower values of $\dot{M}_{\rm acc}$, especially
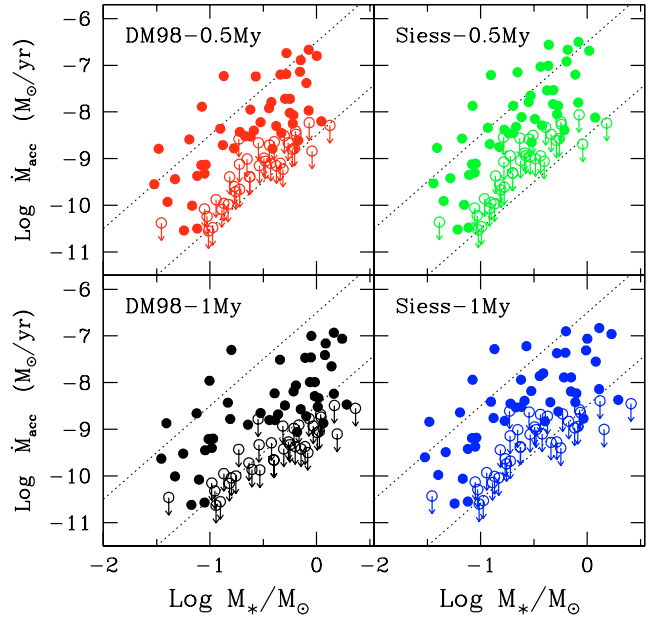
Fig. A.1. Same as Fig. 3 for different ages and evolutionary tracks. The *top-left panel* is for DM98 0.5 My (as in Fig. 3), the *bottom-left* for DM98, 1 My, the *top right* is for Siess (2000) evolutionary tracks at 0.5 My, the *bottom right* at 1 My. In each panel, the two dotted lines ($\dot{M}_{\rm acc} \propto M_\star^2$) have been drawn to guide the eye in the comparison.

for more massive objects, while the range of $M_\star$ remains practically the same. Adopting different evolutionary tracks does not change the results. The main consequence of assuming coeval star formation is to reduce slightly the real spread of $\dot{M}_{\rm acc}$ for any given value of $M_\star$.

Appendix B: Taurus: a test of the method

A validation of the method used to compute the two quantities $\dot{M}_{\rm acc}$ and $M_\star$ and an estimate of the errors can be obtained by applying the same procedure to a sample of objects with known stellar parameters and accretion rates.

The only sample for which this is possible is Taurus, which has been studied extensively over a large range of masses We have taken all the Taurus objects for which we could find in the literature reliable stellar parameters and accretion rates, measured from veiling and/or by fitting the observed Hα profiles with magnetospheric accretion models (Muzerolle et al. 1998a, 2003, 2005; Calvet et al. 2004). For those with published Paβ fluxes or equivalent widths, we have followed the same procedure used for the ρ Oph sample. We have first computed $L_{\rm acc}$ from $L({\rm Pa}\beta)$, and determined the stellar parameters $M_\star/R_\star$ and $M_\star$ from $L_\star$, assuming coeval star formation at 1 My and the DM98 evolutionary tracks. $\dot{M}_{\rm acc}$ is then derived from $L_{\rm acc}$ and $M_\star/R_\star$.

The results are summarized in the Fig. B.1. The top panel shows the complete sample of Taurus objects for which we could find measurements of $\dot{M}_{\rm acc}$ in the literature. The squares are those for which also Paβ data exist; because none of the BDs in Taurus has a published J-band spectrum, we have added the BDs in Ophiuchus and Chamaeleon for which Natta et al. (2004) have measured $\dot{M}_{\rm acc}$ from model fitting of the Hα profiles. The bottom panel shows the same plot when both $M_\star$ and $\dot{M}_{\rm acc}$ are derived from the observed $L_\star$ and Paβ luminosity, as for the ρ Oph stars.
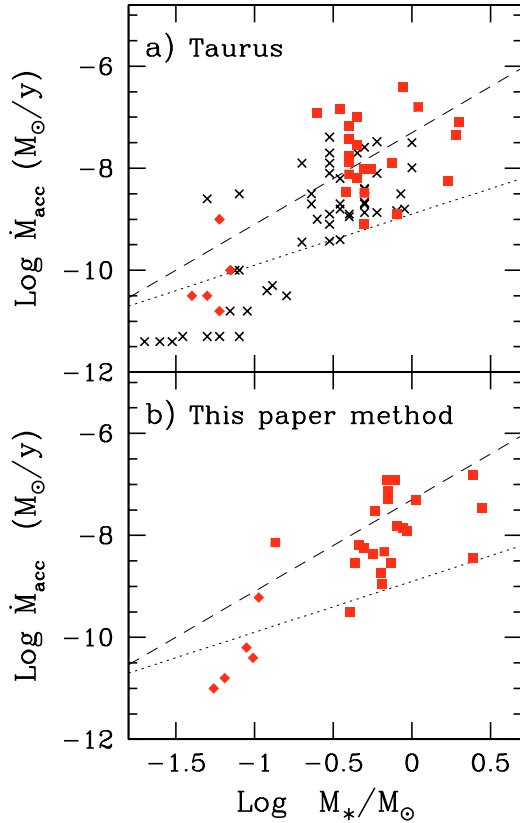
Fig. B.1. *Top panel*: $\dot{M}_{\rm acc}$ vs. $M_\star$ for objects in Taurus for which $\dot{M}_{\rm acc}$ has been obtained from veiling and/or by fitting the Hα profiles with magnetospheric accretion models (crosses and squares). Data from Gullbring et al. (1998), Muzerolle et al. (1998b, 2003, 2005), White & Ghez (2001), White & Basri (2003), Calvet et al. (2004). Squares identify objects for which we could find in the literature Paβ observations. Diamonds are very low mass objects in Ophiuchus and Chamaeleon with $\dot{M}_{\rm acc}$ estimates from Hα profile fitting (from Natta et al. 2004). *Bottom panel*: both $M_\star$ and $\dot{M}_{\rm acc}$ have been derived following the method we use for the Ophiuchus objects in this paper (see text). As in Fig. 3, the two dotted lines show the run of the $\dot{M}_{\rm acc} \propto M_\star^{1.8}$ and $\dot{M}_{\rm acc} \propto M_\star$ relationships.

The results indicate that our procedure does not introduce systematic trends in the results. The trend of $\dot{M}_{\rm acc}$ increasing sharply with $M_\star$ is reproduced in our method, and also the range of $\dot{M}_{\rm acc}$ for a given $M_\star$ is similar, even if, as expected, the assumption of coeval star formation underestimates its spread slightly.

Appendix C: Tables

Tables are available in electronic form only.

References

Alexander, R. D., & Armitage, P. J. 2006, ApJ, 639, L83
Balbus, S. A., & Hawley, J. F. 1991, ApJ, 376, 214
Barsony, M., Koresko, C., & Matthews, K. 2003, ApJ, 591, 1064
Barsony, M., Ressler, M. E., & Marsh, K. A. 2005, ApJ, 630, 381
Bontemps, S., André, Ph., Kaas, A. A., et al. 2001, A&A, 372, 173
Calvet, N., Hartmann, L., & Strom, S. E. 2000, in Protostars and Planets IV, ed. V. Mannings, A. P. Boss, & S. S. Russell (Tucson: University of Arizona Press), 377
Calvet, N., Muzerolle, J., Briceño, C., et al. 2004, AJ, 128, 1294
Cieza, L. A., Kessler-Silacci, J. E., Jaffe, D. T., Harvey, P. M., & Evans, N. J. II 2005, ApJ, 635, 422
D'Antona, F., & Mazzitelli, I. 1997, Mem. S. A. It., 68, 807
Doppmann, G. W., Jaffe, D. T., & White, R. J. 2003, AJ, 126, 3043
Feigelson, E. D., & Nelson, P. I. 1985, ApJ, 293, 192
Gatti, T., Testi, L., Natta, A., & Randich, S. 2006, in preparation
Greene, T. P., & Lada, C. J. 1997, AJ, 114, 2157
Gullbring, E., Hartmann, L., Briceño, C., & Calvet, N. 1998, ApJ, 492, 323
Hartmann, L., Calvet, N., Gullbring, E., & D'Alessio, P. 1998, ApJ, 495, 385
Hueso, R., & Guillot, T. 2005, A&A, 442, 703
Imanishi, K., Koyama, K., & Tsuboi, Y. 2001, ApJ, 557, 747
Johns-Krull, Ch., & Basri, G. 1997, ApJ, 474, 433
Kenyon, S. J., Lada, E. A., & Barsony, M. 1998, AJ, 115, 252
Luhman, K. L., & Rieke, G. H. 1999, ApJ, 525, 440
Meyer, M. R., Calvet, N., & Hillenbrand, L. A. 1997, AJ, 114, 288
Muzerolle, J., Calvet, N., & Hartmann, L. 1998a, ApJ, 492, 743
Muzerolle, J., Hartmann, L., & Calvet, N. 1998b, AJ, 116, 2965
Muzerolle, J., Calvet, N., Briceño, C., Hartmann, L., & Hillenbrand, L. 2000, ApJ, 535, L47
Muzerolle, J., Hillenbrand, L., Calvet, N., Briceño, C., & Hartmann, L. 2003, ApJ, 592, 266
Muzerolle, J., Luhman, K. L., Briceño, C., Hartmann, L., & Calvet, N. 2005, ApJ, 625, 906
Natta, A., Grinin, V. P., & Mannings, V. 2000, in Protostars and Planets IV, ed. V. Mannings, A. P. Boss, & S. S. Russell (Tucson: University of Arizona Press), 559
Natta, A., Testi, L., Comerón, F., et al. 2002, A&A, 393, 597
Natta, A., Testi, L., Muzerolle, J., et al. 2004, A&A, 424, 603
Ozawa, H., Grosso, N., & Montmerle, T. 2005, A&A, 438, 661
Shakura, N. I., & Sunyaev, R. A. 1973, A&A, 24, 337
Siess, L., Dufour, E., & Forestini, M. 2000, A&A, 358, 593
Preibisch, Th., Kim, Y.-C., Favata, F., et al. 2005, ApJS, 160, 401
Ratzka, T., Köhler, R., & Leinert, Ch. 2005, A&A, 437, 611
Scholz, A., & Jayawardhana, R. 2005, ApJ, in press [arXiv:astro-ph/0510629]
Wallace, L. W., Meyer, M. R., Hinkle, K., & Edwards, S. 2000, ApJ, 535, 325
White, R. J., & Basri, G. 2003, ApJ, 582, 1109
White, R. J., & Ghez, A. 2001, ApJ, 556, 265
Wilking, B. A., Meyer, M. R., Robinson, J. G., & Greene, Th. 2005, AJ, 130, 1733

Online Material

Table C.1. Class II objects.

(1)	(2)	(3)	(4)	(5)	(6)	(7)	(8)	(9)	(10)	(11)	(12)	(13)	(14)	(15)	(16)	(17)
#	Object (ISO#)	Coordinates (J2000.0)		J (mag)	H (mag)	K (mag)	A_J (mag)	$\mathrm{Lg}\,L_*$ ($L_\odot$)	$\mathrm{Lg}\,T_{\mathrm{eff}}$ (K)	$\mathrm{Lg}\,M_*$ ($M_\odot$)	EW (Pa_β) (Å)	Inst.	$L(\mathrm{Pa}_\beta)$ ($L_\odot$)	L_{acc} ($L_\odot$)	$\dot{M}_{\mathrm{acc}}$ ($M_\odot$/y)	Other names
1	ρOph-ISO 001	16 25 36.74	−24 15 42.40	10.42	9.04	8.38	1.8	0.21	3.59	−0.26	<−0.7	S	<−4.27	<−1.81	<−8.66	IRS2
2	ρOph-ISO 002+	16 25 38.12	−24 22 36.30	12.84	10.75	9.54	3.1	−0.23	3.53	−0.52	−2.8	S	<−4.07	−1.54	−8.22	B162538-242238
3	ρOph-ISO 003	16 25 39.58	−24 26 34.90	11.89	10.05	8.95	2.5	−0.10	3.55	−0.44	−3.9	S	−3.81	−1.18	−7.92	IRS3
4	ρOph-ISO 006	16 25 56.16	−24 20 48.20	9.15	8.14	7.52	0.5	0.18	3.59	−0.28	−19.0	S	−2.87	0.10	−6.74	SR4/IRS12
5	ρOph-ISO 009	16 26 1.37	−24 25 20.40	14.43	12.44	11.24	2.8	−1.07	3.45	−1.03	<−0.3	I	<−5.74	<−3.80	<−10.24	SKS1-4
6	ρOph-ISO 012	16 26 4.58	−24 17 51.50	15.79	13.41	12.19	4.2	−1.05	3.45	−1.02	<−0.2	I	<−5.96	<−4.11	<−10.55	B162604-241753
7	ρOph-ISO 013	16 26 7.04	−24 27 24.20	15.35	12.38	10.64	5.2	−0.38	3.51	−0.62	−2.1	S	−4.34	−1.90	−8.53	B162607-242725
8	ρOph-ISO 017	16 26 10.33	−24 20 54.80	14.37	10.85	8.47	5.8	0.33	3.61	−0.19	<−0.8	S	<−4.11	<−1.58	<−8.48	GSS26
9	ρOph-ISO 019	16 26 16.84	−24 22 23.20	11.03	9.13	8.20	3.1	0.54	3.64	−0.06	<−0.9	S	<−3.87	<−1.26	<−8.23	GSS29/EL18
10	ρOph-ISO 020	16 26 17.06	−24 20 21.60	9.65	8.61	8.06	0.8	0.10	3.58	−0.33	−1.2	S	−4.15	−1.65	−8.46	DoAr24/GSS28
11	ρOph-ISO 023	16 26 18.82	−24 26 10.50	14.84	13.20	12.14	1.8	−1.69	3.42	−1.40	−1.8	I	−5.59	−3.61	−9.93	SKS1-BDN04
12	ρOph-ISO 024	16 26 18.87	−24 28 19.70	12.58	9.93	8.07	3.7	0.18	3.59	−0.28	−8.9	S	−4.23	−0.35	−7.19	VSSG1
13	ρOph-ISO 026	16 26 20.97	−24 08 51.90	10.88	9.87	9.50	1.0	−0.33	3.52	−0.59	−2.4	I	−3.20	−1.76	−8.41	RBR15
14	ρOph-ISO 030	16 26 21.53	−24 26 1.00	12.57	11.52	10.92	0.7	−1.22	3.44	−1.12	−0.3	I	−5.95	−4.09	−10.50	GY5
15	ρOph-ISO 032	16 26 21.90	−24 44 39.80	12.34	11.48	10.86	0.0	−1.43	3.43	−1.24	−0.4	I	−6.01	−4.17	−10.54	GY3
16	ρOph-ISO 033	16 26 22.27	−24 24 7.10	16.45	15.09	13.94	0.6	−2.95	3.37	−2.16	<−0.7	I	<−7.15	<−5.73	<−11.81	GY11
17	ρOph-ISO 035	16 26 22.96	−24 28 46.10	14.93	12.80	11.53	3.2	−1.12	3.45	−1.06	+0.6	I	—	—	—	GY15
18	ρOph-ISO 036	16 26 23.36	−24 20 59.80	8.97	7.50	6.57	1.5	0.73	3.66	0.05	−0.7	I	−3.80	−1.17	−8.21	GSS31/GY20A
19	ρOph-ISO 037	16 26 23.58	−24 24 39.50	15.05	12.25	10.22	3.9	−0.82	3.46	−0.88	−3.0	I	−4.58	−2.22	−8.71	LFAM3/GY21
20	ρOph-ISO 038	16 26 23.68	−24 43 13.90	9.39	8.40	7.85	0.6	0.13	3.58	−0.31	<−0.5	S	<−4.72	<−2.42	<−9.24	DoAr25/GY17
21	ρOph-ISO 039	16 26 24.04	−24 24 48.10	11.12	8.72	7.32	3.9	0.86	3.68	0.13	<−0.5	S	<−3.83	<−1.20	<−8.29	S2/GY23
22	ρOph-ISO 040	16 26 24.07	−24 16 13.50	10.00	8.09	6.68	2.0	0.53	3.63	−0.07	−12.7	S	−2.72	0.30	−6.67	EL24
23	ρOph-ISO 041	16 26 25.28	−24 24 45.00	16.28	13.10	11.07	5.3	−0.74	3.46	−0.83	<−0.3	I	<−5.50	<−3.48	<−9.98	GY29
24	ρOph-ISO 043	16 26 27.54	−24 41 53.50	11.42	9.98	9.98	4.6	−0.09	3.55	−0.44	<−1.0	I	<−4.39	<−1.97	<−8.71	GY33
25	ρOph-ISO 046	16 26 30.47	−24 22 57.10	16.31	12.55	9.59	6.3	−0.61	3.52	−0.57	<−0.4	S	<−5.27	<−3.16	<−9.71	VSSG27/GY51
26	ρOph-ISO 051	16 26 36.83	−24 15 51.90	12.66	10.83	9.59	2.1	−0.30	3.48	−0.75	−16.5	S	−3.37	−0.58	−7.24	B162636-241554
27	ρOph-ISO 052	16 26 37.79	−24 23 0.70	15.74	12.91	11.11	4.5	−0.86	3.46	−0.90	−5.9	I	<−4.32	<−1.88	<−8.36	VSSG4/GY81
28	ρOph-ISO 053	16 26 38.60	−24 23 10.00	15.29	12.89	11.63	4.2	−0.84	3.46	−0.89	<−0.3	I	<−5.59	<−3.61	<−10.09	GY84
29	ρOph-ISO 056	16 26 41.26	−24 40 18.00	10.77	9.77	9.27	0.8	−0.40	3.51	−0.63	<−0.5	I	<−4.98	<−2.77	<−9.39	WSB37/GY93
30	ρOph-ISO 062	16 26 42.86	−24 20 29.90	10.50	8.77	7.88	2.5	0.53	3.63	−0.07	−1.4	I	−3.68	−1.01	−7.98	GSS37/GY110
31	ρOph-ISO 063	16 26 42.89	−24 22 59.10	15.33	12.82	11.44	4.3	−0.80	3.46	−0.87	<−0.3	I	<−5.50	<−3.47	<−9.96	GY109
32	ρOph-ISO 067	16 26 45.03	−24 23 7.70	13.25	10.60	8.96	4.2	0.09	3.57	−0.33	−10.0	S	<−3.23	−0.40	−7.20	GSS39/GY116
33	ρOph-ISO 068+	16 26 46.43	−24 12 0.10	9.68	8.31	7.49	1.4	0.37	3.61	−0.17	−0.6	S	−4.19	−1.70	−8.61	VSS27
34	ρOph-ISO 072+	16 26 48.98	−24 38 25.20	13.50	11.44	9.98	2.5	−0.81	3.46	−0.87	−36.0	I	−3.49	−0.74	−7.23	WL18/GY129
35	ρOph-ISO 078	16 26 54.44	−24 26 20.70	14.70	11.69	10.01	5.5	0.02	3.57	−0.37	<−0.4	I	<−4.69	<−2.37	<−9.16	VSSG5/GY153
36	ρOph-ISO 079	16 26 54.77	−24 27 2.20	0.00	14.87	12.87	6.0	−1.24	3.44	−1.13	<−3.0	I	—	—	—	GY154
37	ρOph-ISO 083	16 26 56.66	−24 13 53.80	12.26	10.31	9.25	3.0	−0.06	3.56	−0.42	−4.5	I	−3.71	−1.04	−7.79	B162656-241353
38	ρOph-ISO 084	16 26 57.33	−24 35 38.80	0.00	15.09	12.81	7.1	−0.99	3.45	−0.98	<−5.0	S	—	—	—	WL21/GY164
39	ρOph-ISO 086	16 26 58.40	−24 21 30.00	16.01	13.11	11.46	5.1	−0.72	3.47	−0.82	<−0.8	S	<−5.06	<−2.88	<−9.39	IRS26/GY171
40	ρOph-ISO 087	16 26 58.64	−24 18 34.70	15.45	13.01	11.48	3.7	−1.09	3.45	−1.04	−2.4	I	−4.92	−2.69	−9.13	B162658-241836
41	ρOph-ISO 088a	16 26 58.51	−24 45 36.90	9.75	8.16	7.06	1.5	0.40	3.62	−0.14	−10.5	S	−2.92	0.03	−6.90	SR24N/GY168

Table C.1. continued.

(1) #	(2) Object (ISO#)	(3) (4) Coordinates (J2000.0)		(5) J	(6) H (mag)	(7) K	(8) A_J (mag)	(9) Lg L_* ($L_\odot$)	(10) Lg T_{eff} (K)	(11) Lg M_* ($M_\odot$)	(12) $EW(Pa_\beta)$ (Å)	(13) Inst.	(14) $L(Pa_\beta)$ ($L_\odot$)	(15) L_{acc} ($L_\odot$)	(16) $\dot{M}_{acc}$ ($M_\odot/y$)	(17) Other names
42	ρOph-ISO 088b	16 26 58.44	−24 45 31.90	10.37	8.63	7.55	2.1	0.39	3.62	−0.15	−7.0	S	−3.11	−0.23	−7.15	SR24S/GY167
43	ρOph-ISO 089	16 26 59.05	−24 35 56.90	16.05	13.35	11.82	4.7	−0.93	3.46	−0.94	<−0.5	I	<−5.45	<−3.42	<−9.88	WL14/GY172
44	ρOph-ISO 092	16 27 2.34	−24 37 27.20	14.16	10.48	8.06	6.3	0.66	3.65	0.01	−8.4	S	−2.79	0.21	−6.80	WL16/GY182
45	ρOph-ISO 093	16 27 3.01	−24 26 14.70	0.00	15.65	12.56	10.6	−0.24	3.53	−0.53	<−20.0	S	−	−	−	GY188
46	ρOph-ISO 094	16 27 3.59	−24 20 5.40	17.24	14.91	13.56	3.7	−1.90	3.41	−1.53	−5.0	I	−5.34	−3.27	−9.55	B162703-242007
47	ρOph-ISO 095	16 27 4.11	−24 28 29.90	16.90	13.09	10.86	7.2	−0.15	3.54	−0.48	<−0.6	I	<−4.67	<−2.35	<−9.06	WL1/GY192
48	ρOph-ISO 098	16 27 4.57	−24 27 15.70	16.48	13.03	11.22	6.8	−0.17	3.54	−0.49	<−0.7	I	<−4.62	<−2.29	<−9.00	GY195
49	ρOph-ISO 102	16 27 6.60	−24 41 48.80	12.43	11.40	10.77	0.6	−1.22	3.44	−1.12	−2.0	I	−5.12	−2.96	−9.37	GY204
50	ρOph-ISO 103	16 27 6.78	−24 38 15.00	0.00	14.30	10.97	11.6	0.71	3.66	0.04	<−0.6	I	−	−	−	WL17/GY205
51	ρOph-ISO 105	16 27 9.10	−24 34 8.10	12.55	10.19	8.91	4.0	0.29	3.60	−0.21	−1.7	I	−3.82	−1.19	−8.07	WL10/GY211
52	ρOph-ISO 106	16 27 9.07	−24 12 0.80	12.41	10.73	9.80	2.3	−0.44	3.50	−0.65	<−1.0	S	<−4.71	<−2.40	<−9.01	B162708-241204
53	ρOph-ISO 107	16 27 9.35	−24 40 22.40	0.00	13.55	11.30	7.0	−0.30	3.52	−0.56	<−1.3	I	−	−	−	GY213
54	ρOph-ISO 110	16 27 10.28	−24 19 12.70	8.74	7.51	6.72	0.9	0.58	3.64	−0.04	<−0.3	I	<−4.30	<−1.85	<−8.84	SR21/VSSG23
55	ρOph-ISO 112	16 27 11.18	−24 40 46.70	0.00	12.88	10.20	8.9	0.57	3.64	−0.04	−17.9	I	−	−	−	GY224
56	ρOph-ISO 115	16 27 12.13	−24 34 49.10	15.62	13.11	11.49	3.7	−1.16	3.45	−1.08	−2.7	I	−4.94	−2.71	−9.14	WL11/GY229
57	ρOph-ISO 116	16 27 13.73	−24 18 16.90	12.26	10.25	9.29	3.4	0.15	3.58	−0.30	<−1.0	S	<−4.18	<−1.68	<−8.51	B162713-241818
58	ρOph-ISO 117	16 27 13.82	−24 43 31.70	13.32	11.23	9.98	3.1	−0.47	3.50	−0.67	−2.4	S	−4.36	−1.92	−8.52	GY235
59	ρOph-ISO 118	16 27 14.51	−24 26 46.10	0.00	15.34	12.26	10.5	−0.11	3.55	−0.45	<−20.0	I	−	−	−	IRS33/GY236
60	ρOph-ISO 120	16 27 15.45	−24 26 39.80	17.42	13.46	10.79	6.8	−0.57	3.49	−0.73	<−2.5	I	<−4.43	<−2.02	<−8.59	IRS34/GY239
61	ρOph-ISO 121a	16 27 15.88	−24 38 43.40	13.89	11.26	9.59	4.1	−0.25	3.53	−0.53	<−0.6	S	<−4.76	<−2.47	<−9.15	WL20/GY240A
62	ρOph-ISO 121b	16 27 15.70	−24 38 43.40	13.57	10.87	9.48	5.0	0.31	3.60	−0.20	<−0.5	S	<−4.33	<−1.89	<−8.78	WL20/GY240B
63	ρOph-ISO 123	16 27 17.59	−24 5 13.70	12.73	11.49	10.73	1.0	−1.15	3.45	−1.08	−21.9	I	−4.02	−1.46	−7.89	ISO 1627176-240519
64	ρOph-ISO 124	16 27 17.57	−24 28 56.30	0.00	14.42	11.58	9.5	0.03	3.57	−0.37	<−10.0	I	−	−	−	IRS37/GY244
65	ρOph-ISO 128	16 27 18.49	−24 29 5.90	14.61	11.50	9.68	5.5	0.08	3.57	−0.34	<−0.4	S	<−4.63	<−2.30	<−9.10	WL4/GY247
66	ρOph-ISO 129	16 27 19.22	−24 28 43.90	0.00	14.66	11.49	10.9	0.33	3.61	−0.19	<−30.0	I	−	−	−	WL3/GY249
67	ρOph-ISO 132	16 27 21.47	−24 41 43.10	15.22	11.25	8.48	6.6	0.32	3.61	−0.19	<−0.9	S	<−4.06	<−1.52	<−8.42	IRS42/GY252
68	ρOph-ISO 138	16 27 26.22	−24 19 23.00	16.40	14.24	12.93	3.1	−1.79	3.42	−1.46	<−1.0	S	<−5.94	<−4.07	<−10.38	B162726-241925
69	ρOph-ISO 140	16 27 26.49	−24 39 23.10	15.69	12.07	9.95	6.7	0.16	3.58	−0.29	−3.7	S	−3.60	−0.89	−7.72	GY262
70	ρOph-ISO 142	16 27 27.38	−24 31 16.60	12.35	10.38	9.32	3.0	−0.07	3.55	−0.43	<−0.5	S	<−4.67	<−2.35	<−9.10	VSSG25/GY267
71	ρOph-ISO 144	16 27 28.45	−24 27 21.00	15.74	12.31	10.10	5.8	−0.26	3.53	−0.54	<−1.4	I	<−4.40	<−1.98	<−8.66	IRS45/GY273
72	ρOph-ISO 147	16 27 30.18	−24 27 43.40	15.32	11.52	9.02	6.6	0.27	3.60	−0.22	<−0.5	S	<−4.36	<−1.93	<−8.81	IRS47/GY279
73	ρOph-ISO 151	16 27 30.84	−24 24 56.00	12.70	10.95	10.07	2.6	−0.40	3.51	−0.62	<−0.5	S	<−4.97	<−2.76	<−9.39	GY284
74	ρOph-ISO 154	16 27 32.85	−24 32 34.80	16.19	12.74	10.96	6.9	−0.01	3.56	−0.39	<−1.0	S	<−4.32	<−1.88	<−8.65	GY291
75	ρOph-ISO 155	16 27 33.11	−24 41 15.30	11.32	9.13	7.81	3.2	0.49	3.63	−0.09	−4.0	S	−3.26	−0.43	−7.39	GY292
76	ρOph-ISO 160	16 27 37.42	−24 17 54.90	14.15	12.76	11.95	1.5	−1.57	3.43	−1.33	−3.3	I	−5.22	−3.09	−9.44	B162737-241756
77	ρOph-ISO 163	16 27 38.32	−24 36 58.60	11.38	9.43	8.27	2.7	0.23	3.59	−0.25	−2.0	S	−3.80	−1.16	−8.02	IRS49/GY308
78	ρOph-ISO 164	16 27 38.63	−24 38 39.20	13.27	11.93	11.08	1.2	−1.31	3.44	−1.17	−0.8	I	−5.60	−3.61	−10.01	GY310
79	ρOph-ISO 165	16 27 38.94	−24 40 20.70	16.54	13.91	12.29	4.2	−1.35	3.44	−1.20	−9.6	I	−4.56	−2.20	−8.58	GY312
80	ρOph-ISO 166	16 27 39.43	−24 39 15.50	10.75	9.21	8.46	2.2	0.24	3.59	−0.25	−3.3	I	−3.58	−0.87	−7.73	GY314
81	ρOph-ISO 168	16 27 40.29	−24 22 4.00	8.44	7.67	7.21	0.0	0.28	3.60	−0.22	−1.3	S	−3.96	−1.38	−8.26	SR9/GY319/IRS52
82	ρOph-ISO 170	16 27 41.61	−24 46 44.70	17.20	15.33	13.55	1.0	−3.07	3.36	−2.23	<−3.0	S	<−6.63	<−5.01	<−11.07	B162741-244645
83	ρOph-ISO 171	16 27 41.75	−24 43 36.10	0.00	14.88	12.29	8.5	−0.50	3.50	−0.68	<−4.0	I	−	−	−	GY323
84	ρOph-ISO 172	16 27 42.70	−24 38 50.60	13.24	11.44	10.54	2.8	−0.56	3.49	−0.72	<−1.0	S	<−4.82	<−2.56	<−9.12	GY326
85	ρOph-ISO 175	16 27 45.79	−24 44 53.90	17.38	14.54	12.46	4.0	−1.82	3.42	−1.48	−15.7	I	−4.77	−2.49	−8.79	GY344

Table C.1. continued.

(1) #	(2) Object (ISO#)	(3)(4) Coordinates (J2000.0)	(5) J (mag)	(6) H (mag)	(7) K (mag)	(8) A_J (mag)	(9) Lg L_* ($L_\odot$)	(10) Lg $T_{\rm eff}$ (K)	(11) Lg M_* ($M_\odot$)	(12) EW(Pa$_\beta$) / EW(Br$_\gamma$) (Å)	(13) Inst.	(14) L(Pa$_\beta$) / L(Br$_\gamma$) ($L_\odot$)	(15) $L_{\rm acc}$ ($L_\odot$)	(16) $\dot{M}_{\rm acc}$ ($M_\odot$/y)	(17) Other names
86	ρOph-ISO 176	16 27 46.29 −24 31 41.20	13.83	12.21	11.32	2.2	−1.11	3.45	−1.05	<−0.5	I	<−5.62	<−3.64	<−10.08	GY350
87	ρOph-ISO 177	16 27 47.09 −24 45 35.10	15.75	12.81	11.13	5.2	−0.55	3.49	−0.72	<−0.4	I	<−5.21	<−3.09	<−9.66	GY352
88	ρOph-ISO 178	16 27 49.78 −24 25 22.00	12.78	11.12	10.16	2.2	−0.65	3.48	−0.77	−2.0	S	−4.60	−2.25	−8.78	GY371
89	ρOph-ISO 185	16 27 55.25 −24 28 39.60	13.04	11.59	10.79	1.7	−0.98	3.45	−0.97	<−0.2	I	<−5.90	<−4.03	<−10.48	GY397
90	ρOph-ISO 187	16 27 55.58 −24 26 17.90	10.14	9.33	8.90	0.2	−0.39	3.51	−0.62	−5.6	S	−3.91	−1.32	−7.95	SR10/GY400
91	ρOph-ISO 190	16 28 3.56 −24 34 38.60	0.00	15.24	13.20	6.1	−1.37	3.44	−1.21	<−5.0	I	—	—	—	GY450
92	ρOph-ISO 193	16 28 12.72 −24 11 35.60	13.61	12.02	11.09	1.9	−1.11	3.45	−1.05	−1.8	I	−5.07	−2.89	−9.32	B162812-241138
93	ρOph-ISO 194	16 28 13.79 −24 32 49.40	10.98	10.89	10.10	1.8	−0.64	3.48	−0.77	<−0.5	I	<−5.19	<−3.06	<−9.60	B162813-243249
94	ρOph-ISO 195	16 28 16.73 −24 5 14.30	11.31	9.57	8.86	1.8	−0.04	3.56	−0.41	−0.8	S	−4.44	−2.03	−8.79	ISO 1628168-240519
95	ρOph-ISO 196	16 28 16.51 −24 36 58.00	11.31	10.08	9.32	0.9	−0.55	3.49	−0.72	−3.2	S	−4.31	−1.86	−8.43	WSB60/B162816-243657
96	ρOph-ISO 199	16 28 45.60 −24 28 19.00	9.21	8.41	8.00	0.2	0.02	3.57	−0.38	−1.7	S	−4.06	−1.53	−8.31	SR13
97	ρOph-ISO 059	16 26 31.04 −24 31 5.20	14.96	12.32	10.86	4.6	−0.49	3.50	−0.68	<−0.6	S	<−4.06	<−1.54	<−8.13	WL7/GY98
98	ρOph-ISO 070+	16 27 41.61 −24 46 44.70	17.20	15.33	13.55	1.0	−3.07	3.36	−2.23	<−1.2	S	<−4.06	<−3.06	<−9.12	WL2/GY128
99	ρOph-ISO 075	16 26 51.97 −24 30 39.50	0.00	16.52	13.46	10.4	−0.69	3.47	−0.80	<−3.9	S	<−4.06	<−0.40	<−6.92	GY144
100	ρOph-ISO 076	16 26 53.47 −24 32 36.20	0.00	16.24	13.12	10.7	−0.48	3.50	−0.67	<−3.0	S	<−4.06	<−0.32	<−6.92	GY146
101	ρOph-ISO 085	16 26 58.28 −24 37 41.00	0.00	0.00	14.41	−1.0	−0.48	3.50	−0.67	<−8.0	S	—	—	—	CRBR51
102	ρOph-ISO 093	16 26 31.04 −24 31 5.20	0.00	15.65	12.56	10.6	−0.24	3.53	−0.53	<−0.7	S	<−4.06	<−0.73	<−7.41	GY188
103	ρOph-ISO 108	16 27 9.43 −24 37 18.80	16.79	11.05	7.14	10.5	1.44	3.76	0.48	−1.3	S	−4.06	1.46	−5.84	EL29/GY214
104	ρOph-ISO 139	16 27 26.29 −24 42 46.10	0.00	15.18	12.66	8.2	−0.73	3.46	−0.82	<−2.8	S	<−4.06	<−0.77	<−7.27	GY260
105	ρOph-ISO 161	16 27 37.25 −24 42 38.00	0.00	14.52	11.46	10.5	0.27	3.60	−0.22	<−0.8	S	<−4.06	<−0.30	<−7.17	GY301

Column 1: running number; Col. 2: ISOCAM number from BKA01; a + sign marks objects with a companion not resolved in the 2MASS photometry; Cols. 3 and 4: J2000 coordinates; Cols. 5–7: 2MASS J, H, K photometry; Col. 8: J-band extinction; Cols. 9–11: stellar luminosity, effective temperature and mass, determined as described in the text; Col. 12: line equivalent width; negative values for emission lines; Col. 13: instrument used in the observations: S = SOFI/NTT, I = ISAAC/UT1; Col. 14: line luminosity; Cols. 15,16: accretion luminosity and mass accretion rate; Col. 17: other names.

Table C.2. Class III objects.

(1) #	(2) Object (ISO#)	(3) Coordinates (J2000.0)	(4) Coordinates (J2000.0)	(5) J (mag)	(6) H (mag)	(7) K	(8) A_J (mag)	(9) Lg L_* ($L_\odot$)	(10) Lg T_{eff} (K)	(11) Lg M_* ($M_\odot$)	(12) $EW(Pa_\beta)$ (Å)	(13) Inst.	(14) $L(Pa_\beta)$ ($L_\odot$)	(15) L_{acc} ($L_\odot$)	(16) M_{acc} ($M_\odot$/y)	(17) Other names
1	ρOph-ISO 005	16 25 50.53	−24 39 14.50	9.98	8.82	8.33	1.4	0.21	3.59	−0.26	<−0.5	S	<−4.42	<−2.01	<−8.86	IRS10
2	ρOph-ISO 011	16 26 3.29	−24 17 46.50	10.67	9.58	9.12	1.2	−0.18	3.54	−0.49	<−0.8	I	<−4.57	<−2.22	<−8.92	VSSG19
3	ρOph-ISO 014	16 26 7.64	−24 27 41.40	14.68	11.85	10.41	5.4	−0.03	3.56	−0.40	<−0.5	S	<−4.64	<−2.31	<−9.07	B162607-242742
4	ρOph-ISO 016	16 26 9.31	−24 34 12.10	7.74	6.95	6.50	−	−	−	−	+5.7	S	−	−	−	SR3
5	ρOph-ISO 018	16 26 15.81	−24 19 22.10	14.03	11.40	10.03	4.8	−0.02	3.56	−0.40	<−0.5	S	<−4.63	<−2.29	<−9.06	SKS1-7
6	ρOph-ISO 028	16 26 21.02	−24 15 41.50	12.78	10.38	9.27	4.5	0.41	3.62	−0.14	<−0.6	S	<−4.16	<−1.66	<−8.58	B162621-241544
7	ρOph-ISO 044	16 26 28.48	−24 15 41.20	15.31	12.37	10.78	5.4	−0.29	3.52	−0.56	<−0.7	S	<−4.73	<−2.43	<−9.09	B162628-241543
8	ρOph-ISO 064	16 26 43.76	−24 16 33.30	12.98	10.76	9.60	3.8	0.00	3.56	−0.38	<−0.7	S	<−4.46	<−2.07	<−8.84	VSSG11
9	ρOph-ISO 066	16 26 44.30	−24 43 18.00	10.99	10.02	9.57	0.7	−0.51	3.49	−0.69	<−0.8	S	<−4.87	<−2.62	<−9.20	GY112
10	ρOph-ISO 069	16 26 47.05	−24 44 29.90	12.33	11.12	10.56	1.3	−0.83	3.46	−0.89	<−0.4	S	<−5.47	<−3.44	<−9.92	GY122
11	ρOph-ISO 073	16 26 49.23	−24 20 2.90	12.20	9.85	8.69	4.2	0.53	3.63	−0.07	<−0.4	S	<−4.23	<−1.75	<−8.72	VSSG3
12	ρOph-ISO 074	16 26 51.12	−24 20 50.50	13.81	11.48	10.21	−	−	−	−	+1.5	I	−	−	−	IRS20/GY143
13	ρOph-ISO 082	16 26 56.92	−24 28 37.10	17.46	14.75	12.81	3.8	−1.94	3.41	−1.55	<−2.0	I	<−5.77	<−3.85	<−10.12	GY163
14	ρOph-ISO 091	16 27 1.62	−24 21 37.00	14.25	11.07	9.39	6.1	0.49	3.63	−0.09	+0.9	S	−	−	−	VSSG8/GY181
15	ρOph-ISO 113	16 27 11.68	−24 23 42.00	14.21	11.62	10.11	−	−	−	−	+4.0	S	−	−	−	IRS32/GY228
16	ρOph-ISO 114	16 27 11.71	−24 38 32.10	0.00	15.06	11.06	16.2	1.71	3.79	0.64	<−8.0	I	−	−	−	WL19/GY227
17	ρOph-ISO 135	16 27 22.91	−24 17 57.40	13.33	10.76	9.45	−	−	−	−	+1.3	S	−	−	−	WSSG22
18	ρOph-ISO 148	16 27 31.06	−24 34 3.20	13.43	11.36	10.39	3.6	−0.27	3.53	−0.55	<−0.5	S	<−4.86	<−2.61	<−9.28	GY283
19	ρOph-ISO 152+	16 27 32.68	−24 33 23.90	16.15	12.74	10.90	6.6	−0.10	3.55	−0.45	<−2.0	S	<−4.10	<−1.58	<−8.31	GY289
20	ρOph-ISO 156	16 27 35.26	−24 38 33.40	11.28	10.23	9.67	0.8	−0.62	3.48	−0.76	<−0.4	S	<−5.27	<−3.17	<−9.71	GY295
21	ρOph-ISO 158	16 27 36.52	−24 28 33.30	11.99	11.38	11.15	0.0	−1.29	3.44	−1.16	<−1.0	S	<−5.48	<−3.46	<−9.86	GY297
22	ρOph-ISO 169a	16 27 41.49	−24 35 37.70	14.30	11.83	10.56	4.4	−0.30	3.52	−0.57	+0.7	S	−	−	−	GY322
23	ρOph-ISO 169b	16 27 41.64	−24 35 41.10	14.74	12.48	11.26	3.8	−0.78	3.46	−0.85	<−0.9	S	<−5.06	<−2.89	<−9.38	GY322
24	ρOph-ISO 180	16 27 49.87	−24 25 40.20	9.44	8.12	7.30	−	−	−	−	+6.3	S	−	−	−	VSSG14/GY372
25	ρOph-ISO 181	16 27 50.51	−24 39 3.10	14.47	12.74	11.85	−	−	−	−	+5.5	S	−	−	−	GY373
26	ρOph-ISO 183	16 27 51.92	−24 46 29.60	14.05	11.61	10.37	4.3	−0.22	3.53	−0.52	<−0.7	S	<−4.66	<−2.34	<−9.03	GY377
27	ρOph-ISO 186	16 27 55.65	−24 44 50.90	12.34	11.15	10.47	1.0	−0.98	3.45	−0.97	<−1.5	S	<−5.03	<−2.84	<−9.29	GY398
28	ρOph-ISO 189	16 27 57.87	−24 36 2.20	15.37	12.98	11.83	4.4	−0.79	3.46	−0.86	<−1.5	S	<−4.86	<−2.61	<−9.10	GY412
29	ρOph-ISO 192	16 28 5.78	−24 33 55.00	16.75	14.00	12.56	5.1	−1.08	3.45	−1.04	<−2.0	S	<−4.99	<−2.79	<−9.23	GY472
30	ρOph-ISO 197	16 28 21.71	−24 42 47.10	16.83	14.03	12.44	4.9	−1.18	3.45	−1.10	<−1.0	I	<−5.39	<−3.32	<−9.74	B162821-244246
31	ρOph-ISO 198	16 28 32.66	−24 22 44.90	8.73	7.48	6.85	1.3	0.76	3.67	0.07	<−0.4	I	<−4.02	<−1.47	<−8.52	SR20

#	Object (ISO#)	Coordinates (J2000.0)	Coordinates (J2000.0)	J (mag)	H (mag)	K	A_J (mag)	Lg L_* ($L_\odot$)	Lg T_{eff} (K)	Lg M_* ($M_\odot$)	$EW(Br_\gamma)$ (Å)	Inst.	$L(Br_\gamma)$ ($L_\odot$)	L_{acc} ($L_\odot$)	M_{acc} ($M_\odot$/y)	Other names
32	ρOph-ISO 047	16 26 31.04	−24 31 5.20	14.96	12.32	10.86	4.6	−0.49	3.50	−0.68	<−1.0	S	<−4.71	<−1.34	<−7.93	IRS14/GY54
33	ρOph-ISO 113	16 27 11.68	−24 23 42.00	14.21	11.62	10.11	−	−	−	−	+5.6	S	−	−	−	IRS32/GY228
34	ρOph-ISO 157	16 27 35.67	−24 45 32.62	12.71	11.47	10.88	1.4	−0.95	3.46	−0.96	<−1.0	S	<−5.54	<−2.08	<−8.54	GY296
35	ρOph-ISO 179	16 27 49.97	−24 44 17.00	13.85	11.97	10.94	2.8	−0.84	3.46	−0.89	<−0.7	S	<−5.37	<−1.94	<−8.42	GY370

Column 1: running number; Col. 2: ISOCAM number from BKA01; a + sign marks objects with a companion not resolved in the 2MASS photometry; Cols. 3 and 4: J2000 coordinates; Cols. 5−7: 2MASS J, H, K photometry; Col. 8: J-band extinction; Cols. 9−11: stellar luminosity, effective temperature and mass, determined as described in the text; Col. 12: line equivalent width: negative values for emission lines; Col. 13: instrument used in the observations: S = SOFI/NTT, I = ISAAC/UT1; Col. 14: line luminosity; Cols. 15,16: accretion luminosity and mass accretion rate; Col. 17: other names.

Table C.3. Companions not resolved by 2MASS.

(1)	(2)	(3)	(4)	(5)	(6)	(7)	(8)
#	Object	Coordinates		Separation	*EW*	Line	Other
	(ISO#)	(J2000.0)		(arcsec)	(Å)		names
1	ρOph-ISO 002b	16 25 38.12	–24 22 36.30	1.8	<–1.0	Pa$_\beta$	B162538-242238
2	ρOph-ISO 068b	16 26 46.43	–24 12 0.10	3.6	<–0.3	Pa$_\beta$	VSS27
3	ρOph-ISO 070b	16 27 41.61	–24 46 44.70	4	+2.5	Br$_\gamma$	WL2/GY128
4	ρOph-ISO 072b	16 26 48.98	–24 38 25.20	3.6	<–1.0	Pa$_\beta$	WL18/GY129
5	ρOph-ISO 152b	16 27 32.68	–24 33 23.90	3	<–4.0	Pa$_\beta$	GY289